Research Article

Po-Ting Lin, Chan-Sheng Wu, Chun-Hao Peng, Che-Wei Tsai*, and Yutaka S. Sato

Effects of rotational speed on the $Al_{0.3}CoCrCu_{0.3}FeNi$ high-entropy alloy by friction stir welding

https://doi.org/10.1515/htmp-2020-0046
received November 21, 2018; accepted February 12, 2019

Abstract: Welding and relevant studies are indispensable to employ high-entropy alloys for practical applications. In this study, $Al_{0.3}CoCrCu_{0.3}FeNi$ high-entropy alloy with single FCC phase was used to make "bead-on-plate" friction stir welds at different rotational speeds, and the effects on microstructure and mechanical properties were studied. Several banded structures containing oxide or nitride particles were observed in the stir zone (SZ), and the chemical wear of the polycrystalline cubic boron nitride tool was confirmed. The microhardness distribution of the welds showed higher hardness in the SZ because of grain refinement and the presence of deformed grains. The electron backscattered diffraction results suggested that the high-entropy alloy with low stacking-fault energy experienced recrystallization during friction stir welding, which was similar to other conventional materials with low stacking-fault energy.

Keywords: high-entropy alloys, friction stir welding, microstructure

PACS: 81.81.20.-n materials science, methods of materials synthesis and materials processing

*** Corresponding author: Che-Wei Tsai,** Department of Materials Science and Engineering, National Tsing Hua University, 101, Section 2, Kuang Fu Road, Hsinchu, Taiwan; High Entropy Materials Center, National Tsing Hua University, Hsinchu, Taiwan, e-mail: chewei@mx.nthu.edu.tw
Po-Ting Lin: Department of Materials Science and Engineering, National Tsing Hua University, 101, Section 2, Kuang Fu Road, Hsinchu, Taiwan; High Entropy Materials Center, National Tsing Hua University, Hsinchu, Taiwan
Chan-Sheng Wu, Chun-Hao Peng: Department of Materials Science and Engineering, National Tsing Hua University, 101, Section 2, Kuang Fu Road, Hsinchu, Taiwan
Yutaka S. Sato: Department of Materials Processing, Tohoku University, Sendai, Japan

1 Introduction

High-entropy alloys (HEAs) have been attracting considerable attention worldwide since Yeh et al. proposed these materials because of their novel concept and exceptional properties [1]. Numerous studies on HEAs have been conducted, which resulted in a considerable amount of information and the establishment of theories. Miracle and Senkov made a comprehensive review on HEAs and related concepts [2], including the history of development, thermodynamics, taxonomy, microstructures, and various properties. On the other hand, Yeh et al. reviewed the different definitions for HEAs and four core effects of HEAs he proposed earlier [3]. With abundant research on the principles and properties of HEAs being conducted, an important step for the development of HEAs should be on their applications.

Welding plays a crucial role in the applications of alloys. However, only a few studies have investigated the welding of HEAs. Wu et al. studied the weldability of the well-known CoCrFeMnNi HEA using electron beam welding and gas tungsten arc welding [4,5]. Good results were obtained, but the coarse grain structure in the fusion zone might cause negative effects on some applications. Among the various types of welding, friction stir welding (FSW) is a relatively new but promising approach. During FSW, the metal plates are stirred by a plunged rotating tool and joined without melting by tool rotation. Thus, deformation occurs, and recrystallization is activated by friction heat [6]. This welding method has been applied to various structural materials with thorough studies, including Ti–6Al–4V titanium alloy, aluminum alloys, and Inconel alloy 600 [7–9]. FSW is applied to different kinds of alloys because of its special advantages, such as solid-state joining, no requirement for filler materials, and high feasibility of dissimilar welding [10,11].

As for FSW of HEAs, several studies have been conducted. Zhu et al. [12,13] first tested the FSW of $Al_{0.3}CoCrFeNi$ and $Co_{16}Cr_{28}Fe_{28}Ni_{28}$ HEAs at two different welding

Open Access. © 2020 Po-Ting Lin *et al.*, published by De Gruyter. This work is licensed under the Creative Commons Attribution 4.0 International License.

speeds. They studied the cross-sectional microstructure, mechanism of recrystallization, shear texture, and microhardness of the welds. In addition, Jo et al. applied FSW to CoCrFeMnNi [14], and the tensile tests of the welds demonstrated a slight increase in yield strength along with 9% loss in elongation after FSW. All previous results of FSW of HEAs showed good weld appearance without notable defects, which imply the high possibility of using FSW to join HEAs. However, the effects of different rotational speeds on the welds have not yet been determined.

In this study, the aging and precipitation behavior of the newly designed $Al_{0.3}CoCrCu_{0.3}FeNi$ was first elucidated. According to previous studies [15], Al addition has been demonstrated to give rise to the formation of the second phase at room temperature, normally of BCC/B2 structure, in single face-centered cubic (FCC) HEAs. Moreover, the presence of the BCC phase in the FCC matrix can significantly increase the difficulty in processing at room temperature [16]. However, the newly designed $Al_{0.3}CoCrCu_{0.3}FeNi$ HEA was proved to be single FCC [17] and was treated with bead-on-plate FSW at four different rotational speeds from 200 to 500 rpm to further evaluate the weldability of the HEAs under FSW. The microstructure, mechanical properties, grain orientations, and texture of the welds were then examined. In addition, banded structures in the stir zone (SZ), which were also observed in the friction-stir welded $Al_{0.3}CoCrFeNi$ and $Co_{16}Cr_{28}Fe_{28}Ni_{28}$ HEAs [12,13], were examined in this research.

During this research, it was found that microstructure and microhardness of the welds varied based on the traveling distance of FSW (supplementary Figures S1–S3). As a result, given the fact that properties observed at longer traveling distance (farther away from the starting point of welding) should provide more stable and reliable information for applications of FSW with larger scale, all the examined parts of the welds in this study were at least 60–70 mm away from the starting point of welding.

2 Experimental procedure

Ingots of $Al_{0.3}CoCrCu_{0.3}FeNi$ with a size of 40 × 20 × 10 mm^3 were produced by vacuum arc melting with a mixture of constituent elements with purity higher than 99.95 mass% under an argon atmosphere (after a vacuum of 3.3 Pa was reached) at least four times to ensure compositional homogeneity.

To elucidate the aging and precipitation behavior, the ingots were first homogenized at 1,100°C for 6 h (at 1,373 K for 21,600 s), water quenched, and then aged at different temperatures from 400 to 900°C for 1 h (from 673 to 1,173 K for 3,600 s). Then the ingots underwent the Vickers hardness tests with a load of 3 kgf (29.4 N) and a dwelling time of 10 s. X-ray diffraction analysis of the as-homogenized alloy used BRUKER D2 PHASER with Cu-K_α radiation, and the scanning rate was 0.14 degree/s. The alloy was aged at 800°C for 100 h (at 1,073 K for 3,60,000 s) and electro-etched in 30% HNO_3–C_2H_5OH solution to observe the precipitates. For the FSW trials, the arc-melted ingots were cold rolled into 110 × 25 × 3 mm^3 plates (~70% reduction of thickness) and homogenized at 1,100°C for 6 h (at 1,373 K for 21,600 s) and water quenched.

Four bead-on-plate FSW trials were performed at different rotational speeds, i.e., 200, 300, 400, and 500 rpm (Figure 1), with the corresponding Z loads of 35, 30, 21–23, and 20–22 kN. The shoulder diameter, plunge depth, and welding speed were kept constant at approximately 14.3 mm, 2 mm, and 60 mm/min (0.001 m/s), respectively. A Q60 welding tool (MegaStir, USA), consisting of 60% polycrystalline cubic boron nitride (pcBN) and 40% W–25% Re alloy with a convex scrolled shoulder, was used (Figure 2). Argon shielding was employed around the tool during FSW to reduce surface oxidation. The schematic illustration of the bead-on-plate FSW is shown in Figure 3, and the principal directions of the FSW geometry are denoted as normal direction (ND), transverse direction (TD), and welding direction (WD). All the examined parts of the welds were at least 60–70 mm away from the starting point of welding to obtain more stable results.

All microstructural analyses of the welds, including the electron probe microanalysis (EPMA) and electron backscattered diffraction (EBSD), were performed on the ND–TD cross section. The microstructure was examined using a JEOL JSM-IT100 scanning electron microscope equipped with an Oxford x-act energy-dispersive X-ray spectroscopy (EDS) detector. Chemical etching was conducted by immersion in waterless Kalling's etchant (ASTM E 407 designation is 95 Kalling's 2), which consists of 0.5 g of $CuCl_2$, 10 mL of HCl, and 10 mL of C_2H_5OH. The grain

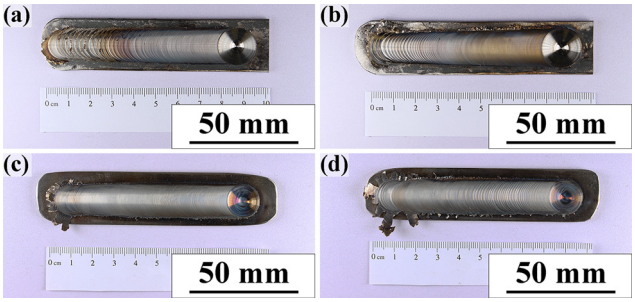

Figure 1: Appearances of the bead-on-plate welds at rotational speeds of (a) 200, (b) 300, (c) 400, and (d) 500 rpm.

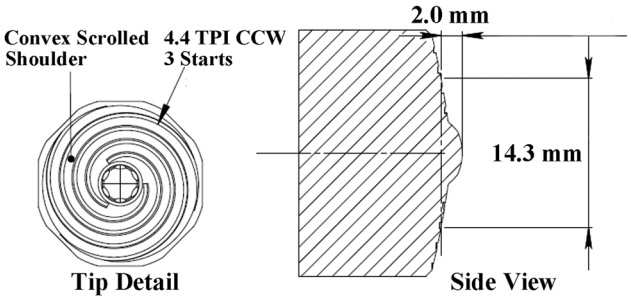

Figure 2: Geometry and dimension of the welding tool.

sizes were measured by ImageJ software. EPMA was conducted using a JEOL JXA-8500F HyperProbe Electron Probe Microanalyzer equipped with eight analyzing crystals capable of analyzing elements from atomic number of 4 (Be) to 92 (U). The oxygen/nitrogen content was analyzed using a HORIBA EMGA-620W oxygen/nitrogen analyzer.

A Mitutoyo hardness testing machine was used for the Vickers hardness tests. A spacing of 0.5 mm, a depth from surface of 0.5 and 1.0 mm, a 0.5 kg (4.9 N) of applied load, and 12 s of dwelling time were used for the microhardness distribution of the welds. The average hardness in the SZ at the depth of 1.0 mm was used to determine the Hall–Petch relationship of the resulting $Al_{0.3}CoCrCu_{0.3}FeNi$ to avoid the influence of surface oxide layer. The Hall–Petch relationship of the annealed $Al_{0.3}CoCrCu_{0.3}FeNi$ was constructed by measuring the average grain size and hardness after cold rolling and annealing at 1,000°C for 2, 5, and 20 h (at 1,273 K for 7,200, 18,000, and 72,000 s).

EBSD analyses were performed using HITACHI SU8010 and JOEL JSM-7800F field emission scanning electron microscopes equipped with Oxford EBSD detectors. The special boundary maps were constructed using a 15° criterion to differentiate the low-angle boundaries (LABs) from the high-angle boundaries (HABs), and the angle of Σ3 boundaries was defined as 60° with the misorientation that satisfies Brandon criterion. The grain misorientation map was constructed using grain-based evaluation criteria, in which a 2° minimum angle θ_c was adopted to define a subgrain. If the internal average misorientation in a grain exceeded θ_c, the grain was classified as deformed. If the internal average misorientation was under θ_c but the misorientation from subgrain to subgrain was above θ_c, then the grain was classified as substructured. Grains with an average internal misorientation lower than θ_c were classified as recrystallized. The inverse pole figures show the orientations of the grains along the ND.

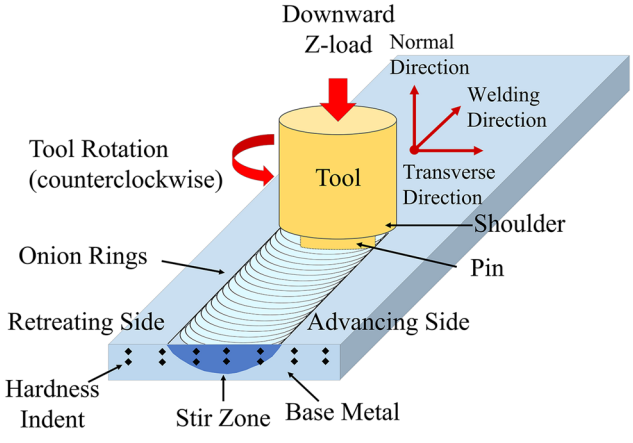

Figure 3: Schematic illustration of bead-on-plate friction stir welding.

3 Results and discussion

3.1 Microstructure of as-homogenized state and as-aged state

After homogenization at 1,100°C for 6 h and water quenching, the XRD pattern of $Al_{0.3}CoCrCu_{0.3}FeNi$ (Figure 4(a)) suggested that the HEA was of single FCC phase. Aging at intermediate temperature (i.e., 600–800°C) for 1 h resulted in the hardening of the HEA (Figure 4(b)). The increase in hardness resulted from precipitation hardening, although the nanoprecipitates were too small to be observed. Thus, prolonged aging was adopted (800°C for 100 h) to analyze the precipitates, and plate-like and spherical precipitates were observed (Figure 4(c)). According to a previous investigation into the precipitation behavior of the $Al_{0.3}CoCrCu_{0.5}FeNi$ HEA by Tsai et al. [18], these precipitates should be rich in Al, Ni, and Cu, with an $L1_2$-ordered FCC structure.

3.2 Microstructure of the plates after welding

The four HEA plates that underwent bead-on-plate FSW showed good appearance and surface integrity with a keyhole (Figure 1). Part of the material was extruded to the surface during the plunging of the tool, and the surface of the HEA plates was subject to oxidation, although argon shielding was employed. The cross sections of the welds showed a typical macrostructure of alloys welded by FSW. The alloys had a basin-shaped SZ at the center

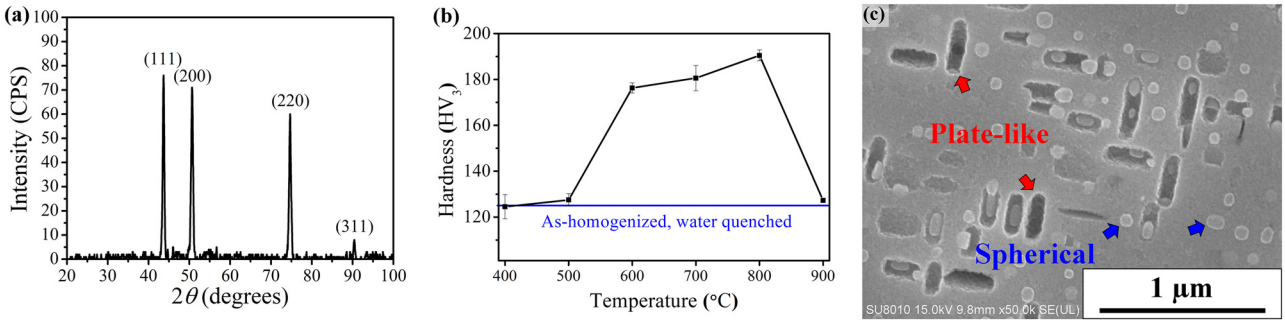

Figure 4: (a) XRD pattern of the as-homogenized $Al_{0.3}CoCrCu_{0.3}FeNi$ high-entropy alloy (HEA). (b) Vickers hardness of the HEA aged at different temperatures for 1 h after homogenization. (c) The microstructure of the HEA after homogenization and aging at 800°C for 100 h showed two types of precipitates.

(circled by red dash lines), a narrow thermal–mechanical-affected zone (TMAZ) enclosing the SZ (unmarked), and the base metal (BM) as delineated in Figure 5(a–d). The grains inside the SZ underwent severe deformation and recrystallization and were thus refined from ~500 μm to less than 10 μm. The refined grain sizes in the SZ were 1.7 ± 0.4 μm (200 rpm), 4.1 ± 1.2 μm (300 rpm), 4.7 ± 1.4 μm (400 rpm), and 6.1 ± 2.2 μm (500 rpm), as measured excluding twins and small deformed grains. The grain size became larger as higher rotational speed was applied, and this phenomenon could be attributed to the higher energy output and friction heat provided for recrystallization and grain growth [6].

Aside from the aforementioned typical macrostructure, several banded structures were also observed in Figure 5(a–d) primarily at the advancing side of the SZ. Fraction of the banded structures decreased with decreasing rotational speed, and the banded structures were hardly observed at 200 rpm. These structures can be classified into bright bands (BBs), dark bands (DBs), and wide bands (WBs). Different kinds of particles, with sizes that usually range from 0.4 to 2 μm, were found at the grain boundaries of these bands. The results from the EDS analysis of the composition of the particles in the banded structures are shown in Table 1. These particles were mainly oxides or nitrides rich in Al with a

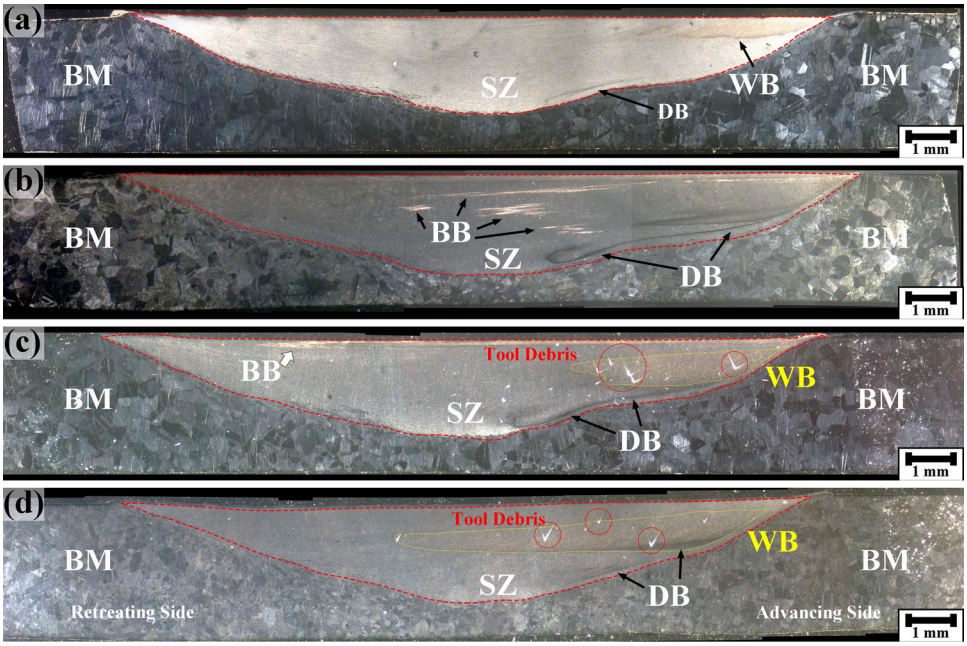

Figure 5: Cross-sectional macrostructure of the welds at rotational speed of (a) 200, (b) 300, (c) 400, and (d) 500 rpm.

Table 1: Energy-dispersive X-ray spectroscopy results of the particles in different banded structures (unit: at%)

Element	N	O	Al	Cr	Fe	Co	Ni	Cu
Bright band (BB)	0	54 ± 9	26 ± 8	9 ± 7	4 ± 3	3 ± 3	3 ± 3	1 ± 1
Dark band (DB)	0	46 ± 8	28 ± 3	7 ± 3	6 ± 3	6 ± 3	5 ± 3	2 ± 1
Wide band (WB)	32 ± 9	0	28 ± 8	10 ± 3	9 ± 3	9 ± 3	9 ± 3	2 ± 1
Base metal (BM)	0	0	6.5	21.7	21.7	21.7	21.7	6.5

comparatively higher content of Cr. Al and Cr are elements with higher chemical activity compared to the others in the BM. Thus, these elements tend to form a compound first, while the HEA is subject to oxidation or other chemical reactions. EPMA was conducted to understand the exact composition of the particles. The results suggested that BB and DB contained mostly Al_2O_3 and a small fraction of Cr_2O_3, but Al_2O_3 and AlN were found in the WB. The EPMA maps presented in Figure 6 show the AlN and Al_2O_3 particles in the WB.

Figure 7(a) shows the microstructure in the normal SZ, in which oval pores were observed at the grain boundaries after chemical etching. After conducting EDS mapping prior to etching, in which the absence of second-phase precipitates was confirmed, and EBSD analyses, which showed small grains surrounded with LABs, these oval pores were believed to be caused by the etching of deformed grains, which are grains not fully recrystallized with higher residual strain. Jo et al. reported a higher fraction of LABs in the SZ compared to other regions of friction-stir-welded CoCrFeMnNi HEA [14]. This result also suggested that the material in the SZ remained deformed after FSW.

The microstructure in the normal SZ were compared to those in BB, DB, or WB (Figure 7(b–d)). Less deformed grains (oval pores) were found in the banded regions. This phenomenon was probably due to the different nucleation mechanisms of recrystallization during FSW. The oxide and nitride particles in the banded structures could serve as additional heterogeneous nucleation sites, which reduced the energy required for recrystallization. This phenomenon resulted in less deformed grains in these

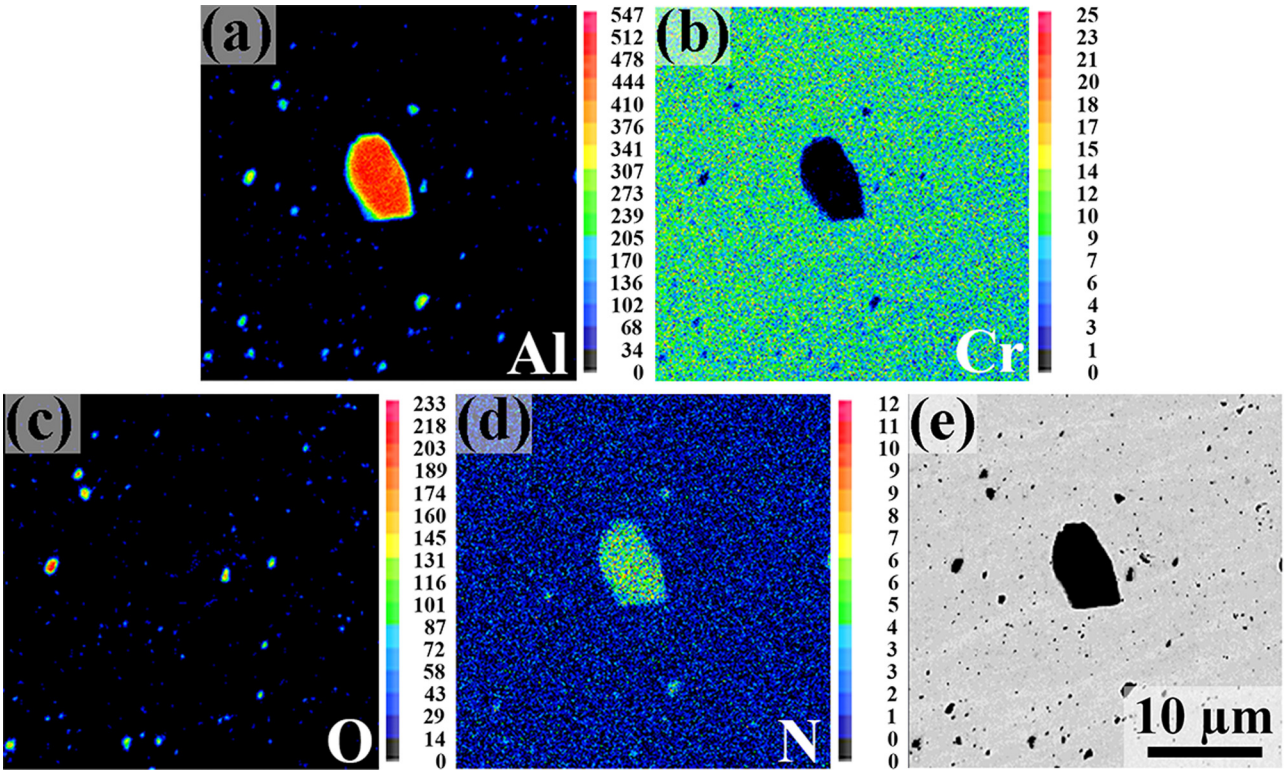

Figure 6: EPMA mapping in the WB showing the spatial distribution of (a) Al, (b) Cr, (c) O, and (d) N and (e) image of backscattered electrons.

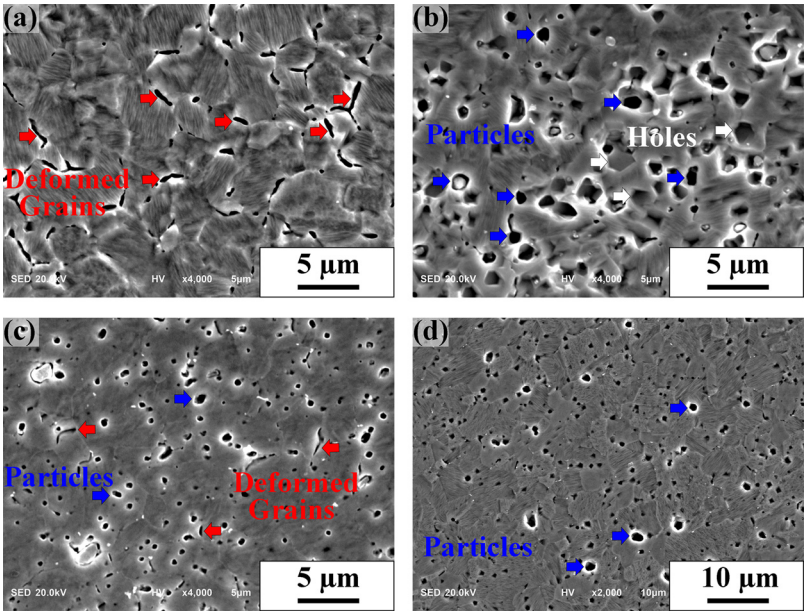

Figure 7: Secondary electron images of the microstructure in the (a) normal SZ, (b) BB, (c) DB, and (d) WB. (a), (b), and (c) are the results at rotational speed of 300 rpm, and (d) is the result at 400 pm.

regions. A similar phenomenon with smaller grain size in the area where particles were dispersed had been reported by Zhu et al. as particle-stimulated nucleation [13].

The formation of BB and DB, in which numerous Al_2O_3 and some Cr_2O_3 particles were found, was speculated to have resulted from the stirring of the surface oxide layer during the FSW. The formation of WB should be related to chemical tool wear, which occurred during FSW and led to some AlN particles, products of chemical reaction between the tool and the HEA, and some tool debris that created deep scratches in the WB (Figure 5(c and d)). The EPMA results showed that the debris consisted of 56.6 ± 1.0 at% B and 43.4 ± 1.0 at% N, which was likely to be pcBN from the tool [19]. These bands appeared mostly on the advancing side because of the mechanisms of material flow during FSW [6]. The flow of materials during FSW can help explain the accumulation of particles at specific locations [20], in this case, the advancing side.

Oxygen/nitrogen analysis of the weld at 300 rpm was performed, and the results are shown in Figure 8(a). The SZ on the advancing side evidently contained higher contents of N and O. The greater content of N supports the suggestion of chemical tool wear, while the higher content of O in the SZ should result from the contribution of oxides in the BB and DB. Park et al. found a similar chemical tool wear in friction-stir-welded austenitic stainless steels using pcBN tool [21].

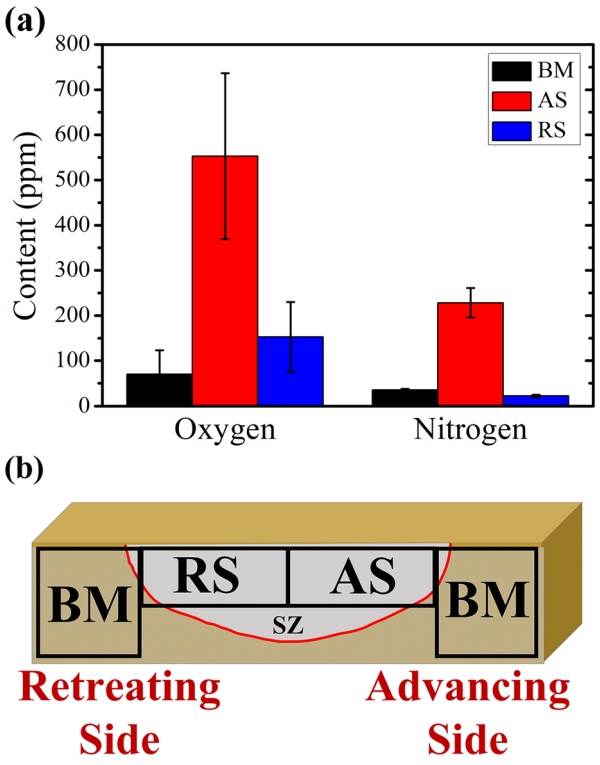

Figure 8: (a) The results of oxygen/nitrogen analysis of the weld at 300 rpm. (b) The schematic illustration of the regions analyzed. (AS: advancing side; RS: retreating side.)

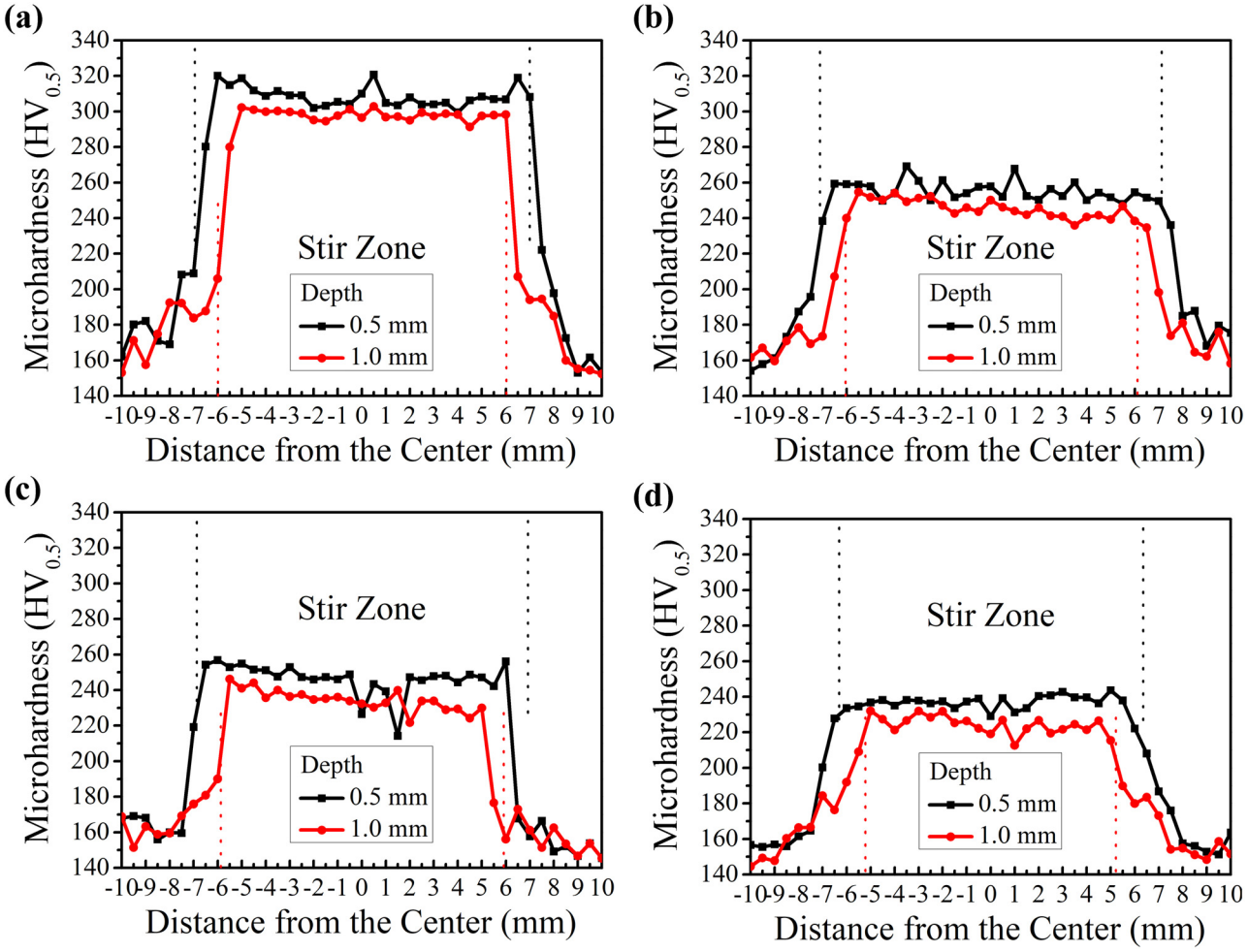

Figure 9: Microhardness distribution of the welds at (a) 200, (b) 300, (c) 400, and (d) 500 rpm. (The dotted lines represent the border of SZ at two depths.)

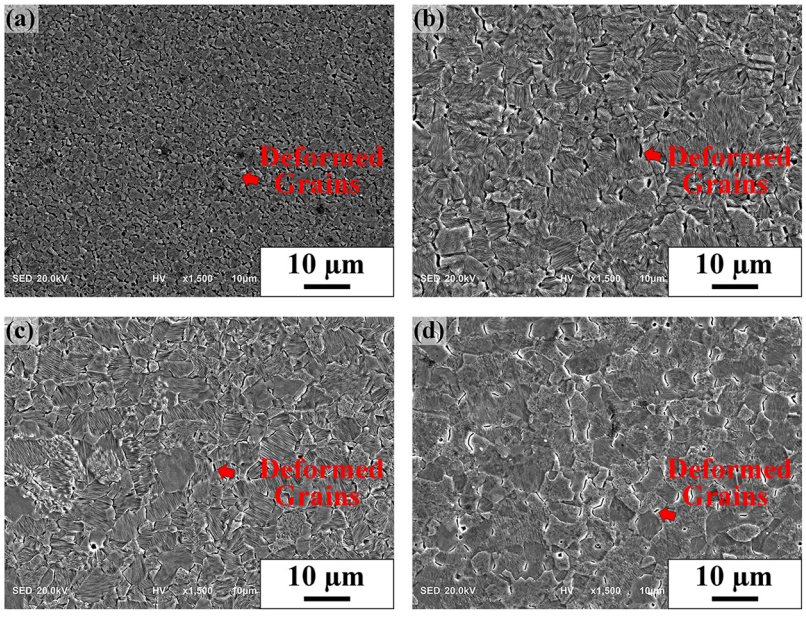

Figure 10: Microstructures in the SZ of the HEA at (a) 200, (b) 300, (c) 400, and (d) 500 rpm after chemical etching.

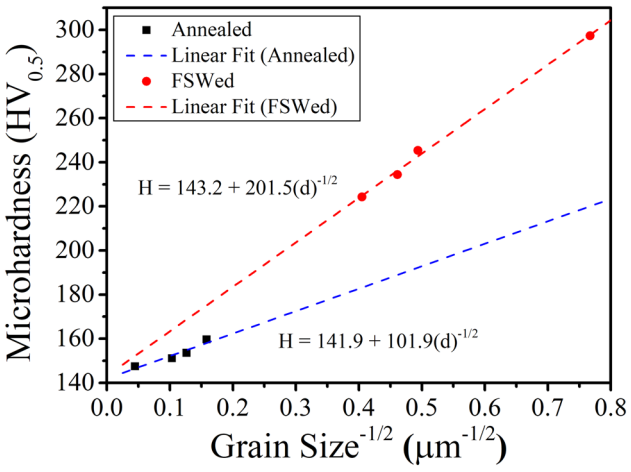

Figure 11: Hall–Petch relationship of the annealed and friction-stir-welded $Al_{0.3}CoCrCu_{0.3}FeNi$.

Table 2: Values of $D(d)$ calculated by equation (1)

Rotational speed (rpm)	Grain size in SZ (μm)	Hardness in SZ ($H_{V0.5}$)	D (d) ($H_{V0.5}$)
200	1.7	297	77
300	4.1	245	53
400	4.7	234	45
500	6.1	224	41

3.3 Mechanical properties of the welds

Figure 9(a–d) show the microhardness distribution at two depths, 0.5 and 1.0 mm, of the welds produced at the different rotational speeds, which clearly reflect the hardening by grain refinement within the SZ. After FSW, the microhardness within the SZ had significantly increased to 220 or above from the original value of the BM (homogenized and water quenched), which is 147 ± 4. The higher hardness at the depth of 0.5 mm, compared to that at the depth of 1.0 mm, was believed to result from the influence of the surface oxide layer, in which oxide particles were dispersed. In addition, the banded structures did not have significant effects on the hardness of the welds, because the advancing side of the weld, where the banded structures were mostly located, did not show higher hardness compared with the retreating side. Comparison of the microhardness results at different rotational speeds showed that higher rotational speed caused larger grain size in the SZ such that the average hardness in SZ would then be lower based on the concept of strengthening/hardening of grain boundaries. However, the contribution of the deformed grains to the hardness should also be considered. As the rotational speed and grain size in the SZ decreased, the number of deformed grains in the SZ apparently increased and became more uniformly distributed, especially when the rotational speed decreased from 300 to 200 rpm (Figure 10). This phenomenon suggests that at lower rotational speed, the SZ of the friction-stir-welded HEA would be more deformed and therefore obtain a higher hardness in addition to the strengthening/hardening effects of grain boundaries. Hence, the revised Hall–-Petch equation for hardness in the SZ of friction-stir-welded $Al_{0.3}CoCrCu_{0.3}FeNi$ should be as follows:

$$H = H_0 + k_H/d^{1/2} + T + D(d) \quad (1)$$

where H is the hardness, H_0 is the materials' intrinsic hardness, k_H is the hardening coefficient, d is the grain size, T is the contribution from twin boundaries, and $D(d)$ represents the hardening from deformed grains and a function of refined grain size.

Sato et al. proposed that Al alloys undergoing FSW tend to have a higher k_H because of the greater density of dislocations in the SZ [22]. Liu et al. reported that CoCrFeMnNi possesses a high hardening efficiency because of the severe lattice distortion effect of HEAs [23], which was proposed by Yeh [3]. Nevertheless, the k_H calculated from the results of the friction-stir-welded $Al_{0.3}CoCrCu_{0.3}FeNi$ with Hall–Petch equation (Figure 11), rather than the revised one, has a value of 201.5 $H_V\mu m^{1/2}$, much higher than 69 $H_V\mu m^{1/2}$ of CoCrFeMnNi calculated by Liu et al. [23] and 90 $H_V\mu m^{1/2}$ of friction-stir-welded $Co_{18}Fe_{28}Ni_{28}Cr_{28}$ calculated by Zhu et al. [13]. The Hall–Petch relationship of the annealed $Al_{0.3}CoCrCu_{0.3}FeNi$ is presented in Figure 11, in which a k_H of 101.9 $H_V\mu m^{1/2}$ and an H_0 of 141.9 were calculated. To explain the higher hardness in SZ and the discrepancy between the FSW and annealing results, the revised Hall–Petch equation, equation (1), should be adopted.

After substituting the parameters of the annealed HEA into the revised Hall–Petch equation (equation (1)) and neglecting the effect of T (based on the EBSD results showing less than 4.06% of Σ3 boundaries in the SZ), the values of $D(d)$ at different rotational speeds can then be solved. The results are shown in Table 2. It shows that $D(d)$ is a decreasing function of rotational speed or grain size. The larger increase in $D(d)$, from 53 to 77, as the rotational speed decreased from 300 to 200 rpm also matches the microstructural observation in Figure 10(a and b), in which the number of deformed grains increased significantly when the rotational speed decreased from 300 to 200 rpm.

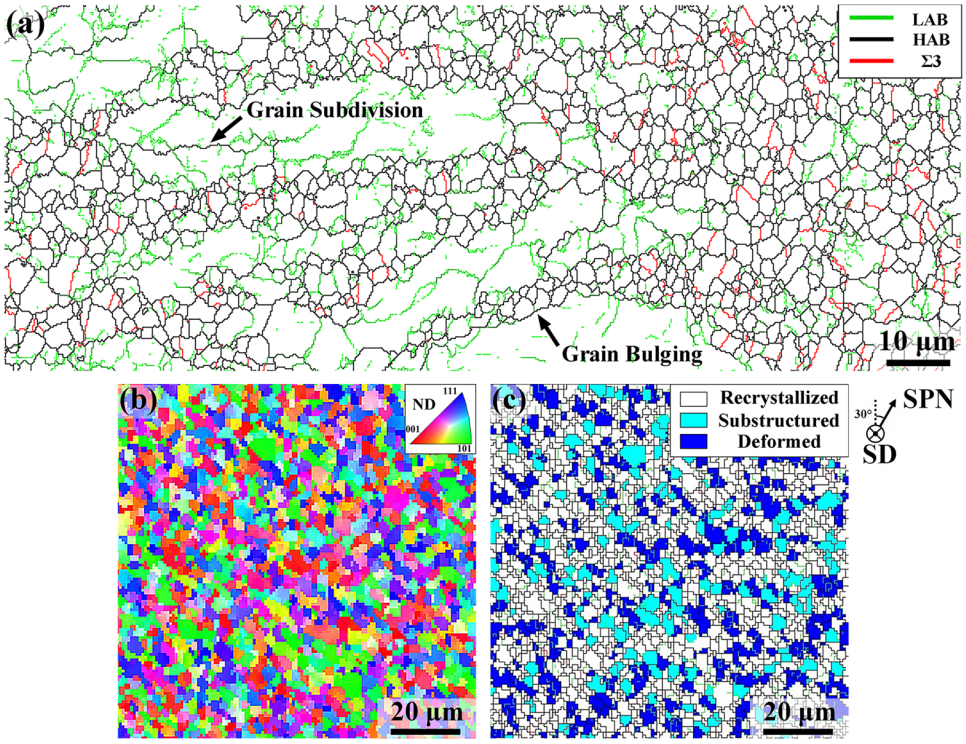

Figure 12: (a) Special boundary map at the edge of the stir zone on the retreating side, (b) inverse pole figure, and (c) misorientation map in the SZ. In (a and c), the LAB, HAB, and Σ3 boundaries are depicted as green, black, and red lines, respectively. For (c), the colors navy blue, light blue, and white represent deformed, substructured, and recrystallized grains, respectively. The shear plane normal (SPN) and the shear direction (SD) of the three figures are as indicated.

3.4 Orientations and texture of grains

EBSD analyses of the weld at 300 rpm were performed to understand the recrystallization and texture developed during FSW. Figure 12(a) shows the special boundary map at the border between SZ and TMAZ on the retreating side. Grain bulging, which is related to discontinuous recrystallization, and grain subdivision, which is related to continuous recrystallization, were observed near the edge of SZ. However, this study could not determine which process was dominant. Figure 12(b and c) show the inverse pole figure and the misorientation map in the SZ on the retreating side. The orientation of the grains in the SZ was quite uniform, but a great number of deformed grains (navy blue) and substructured grains (light blue) remained. This phenomenon again supported the presence of deformed grains in SZ.

The special boundary map of the friction-stir-welded $Al_{0.3}CoCrCu_{0.3}FeNi$ HEA at the border between SZ and TMAZ was similar to that of the friction-stir-welded superaustenitic stainless steel reported by Minorov et al. [24]. However, the refined grains in the SZ of the friction-stir-welded HEA had less Σ3 boundaries or twins. HEAs tend to possess low stacking-fault energy according to the research by Zaddach et al. [25]. This characteristic probably explains the similarity in the special boundary map between the HEA and superaustenitic stainless steel, which also belongs to materials with low stacking-fault energy. Moreover, the similarity of special boundary map between the two alloys suggested that the recrystallization behavior of the HEA during FSW might be dominated by its low stacking-fault energy.

The texture of friction-stir-welded materials is generally accepted to be close to simple shear texture, with the shear direction parallel to the tangent of the probe (pin) [26], which is the part of the tool that plunges into the weld. The {110} and {111} pole figures of the HEA weld at rotational speed of 300 rpm were obtained by analyzing a 500 × 300 μm area in the SZ on the retreating side, approximately 4.3 mm away from the weld center (Figure 13). However, the maximum intensity in the pole figures was only 1.7 multiples of uniform density, which was too low for further discussion of texture formation. The cause of the weak texture in the HEA is currently unknown and requires further study of textural evolution in the HEA during FSW.

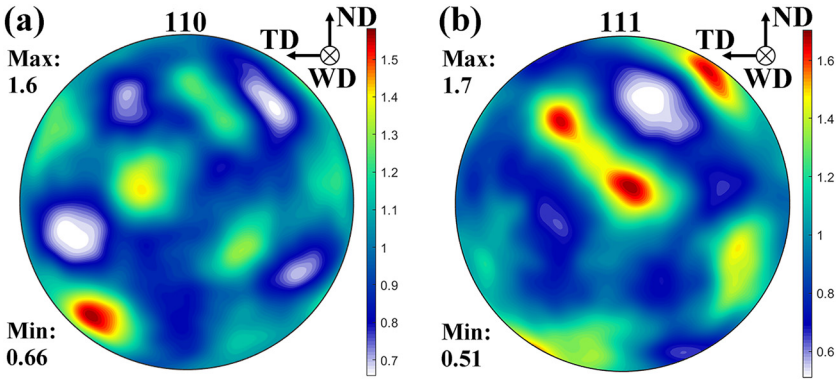

Figure 13: (a) {110}, and (b) {111} pole figures of the weld produced at rotational speed of 300 rpm presented in ND-TD-WD reference frame.

4 Conclusions

The aging and precipitation behavior of the newly designed $Al_{0.3}CoCrCu_{0.3}FeNi$ HEA were examined. The HEA was treated with bead-on-plate FSW at four different rotational speeds, and the welds were analyzed. The following conclusions could be drawn:

1. Aging at intermediate temperature from approximately 600 to 800°C resulted in the precipitation hardening of $Al_{0.3}CoCrCu_{0.3}FeNi$ HEA. The precipitates were deduced to be spherical and platelike, rich in Al, Ni, and Cu, and having $L1_2$ structure.
2. The bead-on-plate welds showed good appearance and typical cross-sectional microstructure of friction-stir-welded alloys (i.e., SZ, TMAZ, and BM). The material in the SZ underwent grain refinement because of the severe deformation and recrystallization during FSW.
3. Deformed grains formed in the SZ because of the insufficient recrystallization, which led to higher hardness in the SZ.
4. Banded structures containing Al_2O_3, Cr_2O_3, or AlN particles, such as BB, DB, and WB, were observed in the SZ and primarily on the advancing side. BB and DB might have formed because of the stirring of the surface oxide layer, while the WB could be the consequence of chemical wear of the pcBN tool. These banded structures did not have significant effects on the microhardness of the welds.
5. The microhardness distribution of the welds reflected hardening in the SZ by grain refinement and the formation of deformed grains. When a higher rotational speed was applied, larger grain size and less deformed grains in the SZ caused lower hardness in the SZ. The revised Hall–Petch relationship is useful in calculating the contribution of grain boundaries and deformed grains to the hardness.
6. The special boundary map at the border between SZ and TMAZ provided evidence of continuous and discontinuous recrystallization, but it was hard to determine which process was dominant during FSW.

Acknowledgments: The present work was supported by the Ministry of Science and Technology grant numbers MOST 109-2634-F-007-024, MOST 108-3017-F-007-002, and MOST 106-2218-E-007-019. The support provided by the High-Entropy Materials Center from the Featured Areas Research Center Program within the framework of the Higher Education Sprout Project by the Ministry of Education in Taiwan is greatly appreciated.

References

[1] Yeh, J. W., S. K. Chen, S. J. Lin, J. Y. Gan, T. S. Chin, T. T. Shun, et al. Nanostructured high-entropy alloys with multiple principal elements: Novel alloy design concepts and outcomes. *Advanced Engineering Materials*, Vol. 6, No. 5, 2004, pp. 299–303.

[2] Miracle, D., and O. Senkov. A critical review of high entropy alloys and related concepts. *Acta Materialia*, Vol. 122, 2017, pp. 448–511.

[3] Yeh, J. W. Physical metallurgy of high-entropy alloys. *JOM-Journal of the Minerals Metals & Materials Society*, Vol. 67, No. 10, 2015, pp. 2254–2261.

[4] Wu, Z., S. A. David, Z. Feng, and H. Bei. Weldability of a high entropy CrMnFeCoNi alloy. *Scripta Materialia*, Vol. 124, 2016, pp. 81–85.

[5] Wu, Z., S. A. David, D. N. Leonard, Z. Feng, and H. Bei. Microstructures and mechanical properties of a welded CoCrFeMnNi high-entropy alloy. *Science and Technology of Welding and Joining*, Vol. 23, No. 7, 2018, pp. 585–595.

[6] Mishra R. S., and Z. Y. Ma, *Materials Science and Engineering R*, Vol. 50, No. 1–2, 2005, pp. 1–78.

[7] Threadgill, P. L., A. J. Leonard, H. R. Shercliff, and P. J. Withers. Friction stir welding of aluminium alloys. *International Materials Reviews*, Vol. 54, No. 2, 2009, pp. 49–93.
[8] Mironov, S., Y. S. Sato, and H. Kokawa. Friction-stir welding and processing of Ti-6Al-4V titanium alloy: A review. *Journal of Materials Science and Technology*, Vol. 34, No. 1, 2018, pp. 58–72.
[9] Sato, Y. S., P. Arkom, H. Kokawa, T. W. Nelson, and R. J. Steel. Effect of microstructure on properties of friction stir welded Inconel Alloy 600. *Materials Science and Engineering A*, Vol. 477, No. 1–2, 2008, pp. 250–258.
[10] Uzun, H., C. D. Donne, A. Argagnotto, T. Ghidini, and C. Gambaro. Friction stir welding of dissimilar Al 6013-T4 To X5CrNi18-10 stainless steel. *Materials Design*, Vol. 26, No. 1, 2005, pp. 41–46.
[11] Sato, Y. S., H. Kokawa, H. T. Fujii, Y. Yano, and Y. Sekio. Mechanical properties and microstructure of dissimilar friction stir welds of 11Cr-ferritic/martensitic steel to 316 stainless steel. *Metallurgical and Materials Transactions. A, Physical Metallurgy and Materials Science*, Vol. 46A, No. 12, 2015, pp. 5789–5800.
[12] Zhu, Z. G., Y. F. Sun, M. H. Goh, F. L. Ng, Q. B. Nguyen, H. Fujii, et al. Friction stir welding of a CoCrFeNiAl0.3 high entropy alloy. *Materials Letters*, Vol. 205, 2017, pp. 142–144.
[13] Zhu, Z. G., Y. F. Sun, F. L. Ng, M. H. Goh, P. K. Liaw, H. Fujii, et al. Friction-stir welding of a ductile high entropy alloy: Microstructural evolution and weld strength. *Materials Science and Engineering A*, Vol. 711, 2018, pp. 524–532.
[14] Jo, M. G., H. J. Kim, M. Kang, P. P. Madakashira, E. S. Park, J. Y. Suh, et al. Microstructure and mechanical properties of friction stir welded and laser welded high entropy alloy CrMnFeCoNi. *Metals and Materials International*, Vol. 24, No. 1, 2018, pp. 73–83.
[15] Kumar, J., N. Kumar, S. Das, N. Gurao, and K. Biswas. Effect of Al addition on the microstructural evolution of equiatomic CoCrFeMnNi alloy. *Transactions of the Indian Institute of Metals*, Vol. 71, No. 11, 2018, pp. 2749–2758.
[16] Wani, I., G. D. Sathiaraj, M. Ahmed, S. Reddy, and P. P. Bhattacharjee. Evolution of microstructure and texture during thermo-mechanical processing of a two phase Al0.5CoCrFeMnNi high entropy alloy. *Materials Characterization*, Vol. 118, 2016, pp. 417–424.
[17] Wu, C. S., P. H. Tsai, C. M. Kuo, and C. W. Tsai. Effect of atomic size difference on the microstructure and mechanical properties of high-entropy alloys. *Entropy* (*Basel, Switzerland*), Vol. 20, No. 12, 2018, pp. 967.
[18] Tsai, M. H., H. Yuan, G. Cheng, W. Xu, K. Y. Tsai, C. W. Tsai, et al. Morphology, structure and composition of precipitates in $Al_{0.3}CoCrCu_{0.5}FeNi$ high-entropy alloy. *Intermetallics*, Vol. 32, 2013, pp. 329–336.
[19] Zhang, Y., Y. S. Sato, H. Kokawa, S. H. C. Park, and S. Hirano. Stir zone microstructure of commercial purity titanium friction stir welded using pcBN tool. *Materials Science and Engineering A*, Vol. 488, No. 1–2, 2008, pp. 25–30.
[20] Ma, Z. Y., S. R. Sharma, and R. S. Mishra. Effect of friction stir processing on the microstructure of cast A356 aluminum. *Materials Science and Engineering A*, Vol. 433, No. 1–2, 2006, pp. 269–278.
[21] Park, S. H. C., Y. S. Sato, H. Kokawa, K. Okamoto, S. Hirano, and M. Inagaki. Boride formation induced by pcBN tool wear in friction-stir-welded stainless steels. *Metallurgical and Materials Transactions. A, Physical Metallurgy and Materials Science*, Vol. 40, No. 3, 2009, pp. 625–636.
[22] Sato, Y. S., S. H. C. Park, and H. Kokawa. Microstructural factors governing hardness in friction-stir welds of solid-solution-hardened Al alloys. *Metallurgical and Materials Transactions. A, Physical Metallurgy and Materials Science*, Vol. 32, No. 12, 2001, pp. 3033–3042.
[23] Liu, W. H., Y. Wu, J. Y. He, T. G. Nieh, and Z. P. Lu. Grain growth and the Hall–Petch relationship in a high-entropy FeCrNiCoMn alloy. *Scripta Materialia*, Vol. 68, No. 7, 2013, pp. 526–529.
[24] Mironov, S., Y. S. Sato, H. Kokawa, H. Inoue, and S. Tsuge. Structural response of superaustenitic stainless steel to friction stir welding. *Acta Materialia*, Vol. 59, No. 14, 2011, pp. 5472–5481.
[25] Zaddach, A. J., C. Niu, C. C. Koch, and D. L. Irving. Mechanical properties and stacking fault energies of NiFeCrCoMn high-entropy alloy. *JOM-Journal of the Minerals Metals & Materials Society*, Vol. 65, No. 12, 2013, pp. 1780–1789.
[26] Fonda, R. W., and K. E. Knipling. Texture development in friction stir welds. *Science and Technology of Welding and Joining*, Vol. 16, No. 4, 2011, pp. 288–294.